Check for updates

Advanced Materials Technologies

ADVANCED MATERIALS TECHNOLOGIES
www.advmattechnol.com

RESEARCH ARTICLE OPEN ACCESS

Skin-Like Tri-Modal Sensors Based on Soft Piezoelectric and Ionic Composites

Liren Wang[1,2,3] | Peter Zalar[4] | Vishva Bhate[1,2] | Takeo Furukawa[5] | Hidekazu Kodama[5] | Yijun Liu[1,2] | Yuanyuan Zhou[1,2] | Chuang Hou[1,2] | Siyuan Liu[1,2] | Naoji Matsuhisa[1,2,3]

[1]Research Center for Advanced Science and Technology (RCAST), The University of Tokyo, Meguro-ku, Tokyo, Japan | [2]Institute of Industrial Science, The University of Tokyo, Meguro-ku, Tokyo, Japan | [3]Department of Electronics and Electrical Engineering, Keio University, Yokohama, Kanagawa, Japan | [4]High Tech Campus 31, Holst Centre/TNO, Eindhoven, Netherlands | [5]Kobayasi Institute of Physical Research, Kokununji, Tokyo, Japan

Correspondence: Peter Zalar (peterzalar@gmail.com) | Naoji Matsuhisa (naoji@iis.u-tokyo.ac.jp)

Received: 18 December 2025 | **Revised:** 10 February 2026 | **Accepted:** 3 March 2026

Keywords: multimodal sensor | piezoelectric-ionic composite | stretchable electronics

ABSTRACT

Human skin perceives complex external stimuli through the coordinated detection of temperature, static strain, and dynamic strain. However, current skin-like multimodal sensors are typically limited to dual-mode sensing or suffer from signal interference and excessive wirings. In this study, a soft, skin-like tri-modal sensor capable of independent and simultaneous detection of temperature, static strain, and dynamic strain is reported. The sensor consists of a single, skin-inspired sensing layer of a soft, piezoelectric and ionic composite film that is sandwiched between stretchable electrodes. It uses distinct frequency-domain responses: charge relaxation time for temperature, normalized capacitance for static strain, and piezoelectric charge output for dynamic strain—to fully decouple signals without the need for separate sensors. Practical demonstrations include simultaneous detection of skin temperature and pulse waves at the wrist, localized mapping of strain and temperature under shear stress, and texture recognition through dynamic force sensing. This work provides a compact and scalable platform for fully decoupled tri-modal sensing, paving the way for intelligent prosthetics, on-skin electronics, and interactive robotics.

1 | Introduction

Skin's multimodal sensing ability enables the simultaneous detection of temperature, slow deformation (static strain), and fast vibration (dynamic strain) [1–4]. The simultaneous perception of multiple signals is essential for understanding the nature of external contact [5], monitoring physiological conditions [6], and adjusting motor responses [7, 8]. For example, when doctors place their hands on a patient's body, they integrate multiple signals—such as temperature, softness, texture, and pulse waves—to formulate an accurate diagnosis. Similarly, wearable multimodal healthcare sensors enable timely diagnosis and targeted rehabilitation strategies for conditions like hypertension or muscle degeneration [9–11]. In intelligent robotics or prosthetics, multimodal sensors enhance dexterous object manipulation [12–14].

Designing multimodal sensors requires sensing of various signals and their decoupling. One common approach is incorporating multiple independent sensing units into a single system to detect different stimuli simultaneously [10, 12, 14–18]. For instance, multimodal electronic skins were realized by multiple metal films with different structures which have different sensitivity in temperature and pressure [12]. Another approach is to utilize materials responsive to multiple stimuli and decouple the signals at readout. For example, ion-gel based multimodal sensing has been realized, which is assisted by additional signal processing strategies for signal decoupling [19–21]. Reliable signal

This is an open access article under the terms of the Creative Commons Attribution License, which permits use, distribution and reproduction in any medium, provided the original work is properly cited.

© 2026 The Author(s). *Advanced Materials Technologies* published by Wiley-VCH GmbH

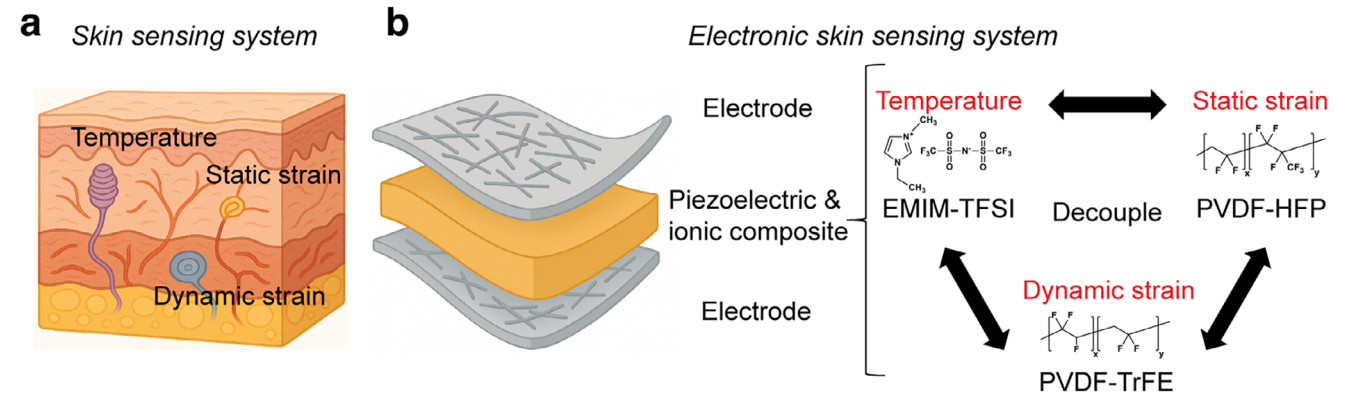


FIGURE 1 | Conceptual framework of a multimodal artificial sensing system for signal decoupling inspired by human skin. (a) Illustration of natural skin structure showing spatial distribution of temperature, static strain, and dynamic strain sensing modalities. (b) Multilayer composite design of the multimodal sensor, where PVDF-TrFE is used for dynamic strain sensing, PVDF-HFP for static strain sensing, and EMIM-TFSI for temperature sensing.

decoupling based on physics has been achieved by utilizing different electrical parameters to independently monitor distinct stimuli within a single device [13, 22–26]. A previous report decouples the sensing of temperature and static strain based on ion relaxation dynamics [13]. By eliminating the need for additional sensing units, this approach effectively reduces wiring complexity and enhances system integration.

However, the number of skin-like multimodal perceptions in a single sensor unit has been limited to only two, although our skin perceives more to realize collaborative perception. The main challenge is how to integrate additional orthogonal sensing mechanisms without adding structural complexity or introducing signal interference. Therefore, we looked into utilizing time-domain measurements. Ion-relaxation-based multimodal sensors detect temperature and static strain from impedance spectra in a frequency range of ~10^3–10^5 Hz [27], suggesting low-frequency signals do not affect the signal. Achieving a low-frequency electrical property whose temperature dependence is practically negligible relative to other effects is critical for enabling additional sensing modalities. In addition, mechanoreceptors in skin are soft, ionic, and capable of piezoelectric transduction, converting mechanical stress into electrical signals [28, 29]. Inspired by this, we hypothesized piezoelectricity would enable an additional sensing mode.

Here, we show a skin-like tri-modal sensor for temperature, static strain, and dynamic strain determination, made of a soft ionic and piezoelectric composite sandwiched between stretchable electrodes. Our sensor replicates the multifunctional capabilities of human skin, which relies on distinct thermoreceptors, mechanoreceptors, and nociceptors for temperature, static pressure, and dynamic mechanical vibrations, respectively (Figure 1). It effectively decouples temperature, static strain, and dynamic strain using frequency domain measurements. The multimodal sensing capability allows accurate temperature and strain mapping, which is essential for real-time physiological monitoring and artificial tactile sensing. By integrating the sensor into prosthetic fingers, we demonstrate its ability to detect physiological signals such as body temperature and heart rate, highlighting its potential in wearable health monitoring.

2 | Fabrication of the Multimodal Sensor and the Characteristic of the Piezoelectric-Ionic Composite Film

The multimodal sensor comprises a functional composite sensing layer sandwiched between stretchable electrodes. The stretchable electrodes are based on highly conductive silver nanowires embedded in elastic styrene-ethylene-butylene-styrene (SEBS) [13]. The sensing active layer is a 4-μm-thick composite film, integrating the piezoelectric copolymer, poly (vinylidene fluoride-trifluoro ethylene) (PVDF-TrFE), a fluorinated elastomer, poly (vinylidene fluoride-co-hexafluoropropylene) (PVDF-HFP), and an ionic conductor, 1-ethyl-3-methylimidazolium bis(trifluoromethylsulfonyl)imide (EMIM-TFSI) (Figure 1B). The detailed manufacturing process of the sensor is shown in Figure S1. Similar to how human skin integrates different receptors for comprehensive sensory feedback, the sensor utilizes multiple physical mechanisms to detect various stimuli simultaneously. PVDF-TrFE detects dynamic strain via the piezoelectric effect, PVDF-HFP functions as a dielectric medium for capacitive-based static strain sensing, and EMIM-TFSI enables temperature sensing through impedance variations [27, 30]. By leveraging charge relaxation time [31], normalized capacitance, and piezoelectric output, tri-modal sensing is effectively realized.

We first examined the influence of each component's concentration on the mechanical and electrical properties of the composite films. Figure 2a shows the effect of the mixing ratio of PVDF-TrFE and PVDF-HFP in the stretchability and piezoelectric constant. The concentration of EMIM-TFSI was fixed at 5.0 wt.%. The stretchability was characterized by crack onset strain, which marks the initiation of microcracks under tensile strain [32, 33]. The crack onset strain of neat PVDF-TrFe was only 20%, and that of the composite (PVDF-TrFE: PVDF-HFP = 1:1 (w:w)) was enhanced to 75%. The optical microscope images of the composite films under different strains are shown in Table S1. As the PVDF-HFP ratio increased, the piezoelectric coefficient (d_{33}) decreased. Neat PVDF-TrFE showed a d_{33} of 25 pC N^{-1} while the PVDF-TrFE: PVDF-HFP (1:3) had a d_{33} of 4.2 pC N^{-1}. This observation agrees with a previous report on the composite of PVDF-TrFE and elastomers without ionic liquids [34].

2365709x, 0, Downloaded from https://advanced.onlinelibrary.wiley.com/doi/10.1002/admt.202502649 by Tno Ris, Wiley Online Library on [05/05/2026]. See the Terms and Conditions (https://onlinelibrary.wiley.com/terms-and-conditions) on Wiley Online Library for rules of use; OA articles are governed by the applicable Creative Commons License

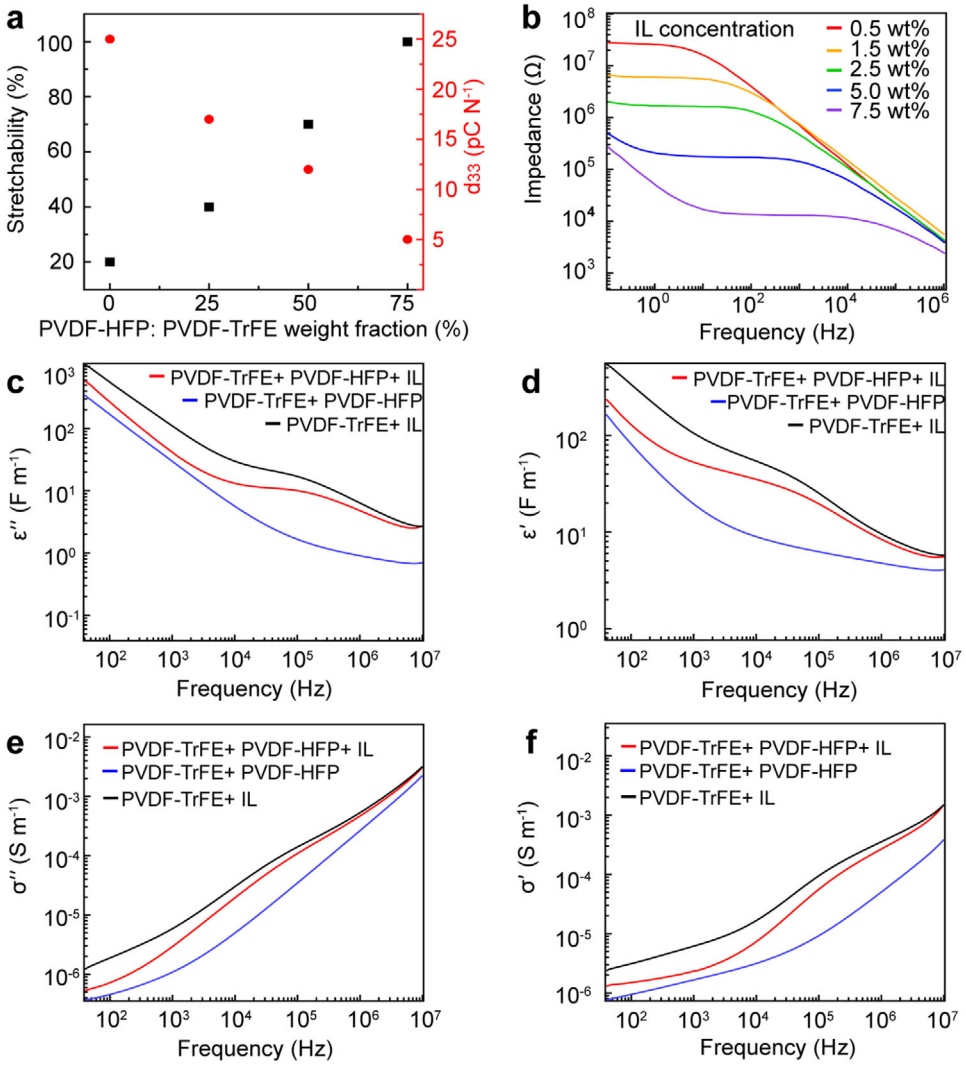


FIGURE 2 | Characterization of mechanical and electrical properties of composite films composed of PVDF-TrFE, PVDF-HFP, and ionic liquid (IL, EMIM-TFSI). (a) Variation of stretchability and piezoelectric coefficient d_{33} as a function of PVDF-HFP weight fraction. (b) Frequency-dependent impedance spectra of composite films with varying IL concentrations (0.5–7.5 wt.%). (c–f) Broadband dielectric and conductivity analysis of three representative composite configurations: PVDF-TrFE + PVDF-HFP + IL, PVDF-TrFE + PVDF-HFP, and PVDF-TrFE + IL. (c) Imaginary part of electrical permittivity (ε''); (d) Real part of electrical permittivity (ε'); (e) Imaginary part of electrical conductivity (σ''); (f) Real part of electrical conductivity (σ'). These results demonstrate the synergistic effects of blending PVDF-HFP and IL on both stretchability and ionic-electronic transport performance.

Figure S2 shows the ionic conductivity of the composite films with different PVDF-TrFE/PVDF-HFP compositions. The concentration of EMIM-TFSI was fixed at 5.0 wt.%. With increasing PVDF-HFP content from 0% to 100% in PVDF-TrFE/PVDF-HFP, the ionic conductivity increased from 8.1×10^{-10} S cm^{-1} to 3.0×10^{-8} S cm^{-1}. The enhanced ionic conductivity is attributed to the more amorphous nature of PVDF-HFP, which provides increased free volume and improved ion mobility compared to PVDF-TrFE. In summary, the PVDF-TrFE: PVDF-HFP (1:1) composite resulted in an optimal balance between mechanical stretchability (70%), which is larger than nominal strain in human skin, higher ionic conductivity (5.0×10^{-9} S cm^{-1}) and a relatively high piezoelectric coefficient of 12 pC N^{-1}.

The effect of ionic liquid content in the composite was first evaluated by the crack onset strain. As the ionic liquid content increased from 0.5 wt.% to 7.5 wt.%, the crack onset strain increased from 40% to 70%, indicating ionic liquid worked as a plasticizer (Figure S3). In addition, the piezoelectric coefficient d_{33} of the composite films increased monotonically from 9.9 pC N^{-1} at 0.5 wt.% to 16.1 pC N^{-1} at 7.5 wt.% (Figure S3f). The increased d_{33} in the presence of the ionic liquid may be attributed to the enhancement of β-Phase crystalline structure of PVDF [35]. Figure 2b shows impedance spectroscopy of composite films with varying ionic liquid concentrations (0.5–7.5 wt.%). As the ion concentration increases, the low frequency impedance of the composite decreased significantly. Low ion concentrations were found to enhance temperature sensitivity by increasing the activation energy of ionic conductivity, enabling more sensitive detection of temperature changes [13]. At 5.0 wt.%, the relatively high resistance of the composite provided a significant impedance difference from the stretchable silver-nanowires-based electrodes, enhancing the sensitivity and stability of the sensor performance. In addition, both resistance

2365709x, 0, Downloaded from https://advanced.onlinelibrary.wiley.com/doi/10.1002/admt.202502649 by Tno Ris, Wiley Online Library on [05/05/2026]. See the Terms and Conditions (https://onlinelibrary.wiley.com/terms-and-conditions) on Wiley Online Library for rules of use; OA articles are governed by the applicable Creative Commons License

(R) and capacitance (C) of the composite can be accurately measured within the instrument's accessible frequency range (10^{-1}–10^{6} Hz). Therefore, an ion concentration of 5 wt.% was used in the following study. The composite film (PVDF-TrFe: PVDF-HFP: EMIM-TFSI = 10: 10: 1) was observed using atomic force microscopy (AFM) and showed uniform morphology (Figure S4).

The morphologies of the composite films, such as polymer polarization behavior and ion migration were systematically analyzed by impedance spectroscopy (Figure 2c–f). To clarify the role of each component, three systems were investigated: PVDF-TrFE + PVDF-HFP + EMIM-TFSI (PPE) (10:10:1, w:w), PVDF-TrFE + PVDF-HFP (PP) (1:1, w:w), and PVDF-TrFE + EMIM-TFSI (PE) (20:1, w:w). All composite sensing films were contact poled under a DC electric field of 100 MV/m, and the thickness of each sensing film was kept at 4 μm.

Figure 2c,d present the imaginary part (ε'') and real part (ε') dielectric constants of three polymer composite systems at different frequencies. The electrical behavior of ionic conductors exhibits a significant frequency dependence. In the low frequency regime (10^{2}–10^{4} Hz), the dielectric response is dominated by the ionic electrical double layer near the electrodes, which makes the apparent dielectric constant high. At high frequencies (>10^{4} Hz), the dielectric properties are determined by the orientation polarization of nonionic molecules, due to the slow response of ions to the alternating electric field [27, 31]. In the low frequency range (10^{2}–10^{4} Hz), the PE system exhibits the highest dielectric constant. The internal polarizing electric field causes a significant ion migration and the accumulation around electrodes to form electrical double layer capacitance. PPE system shows an intermediate dielectric constant because the internal polarizing electric field is diluted by non-piezoelectric PVDF-HFP. The PP system showed the lowest dielectric constant due to its lack of ionic liquids, and its dielectric response mainly comes from the orientation polarization of polar groups on the polymer chains. In the high-frequency regime (>10^{4} Hz), the dielectric constant shows a gradual and more stable decline, indicating a change in the dominant polarization mechanism. The decrease in ε' and ε'' indicates the occurrence of the polarization lag phenomenon. Outside this frequency range, the dielectric response is mainly determined by the dipole orientation rather than the ionic displacement. The ionic mobility is insufficient to follow the rapidly alternating electric field. This transformation reflects the transition from ionic conduction to dielectric polarization, which can be effectively described by a parallel RC circuit model.

Figure 2e,f display the corresponding frequency-dependent imaginary (σ'') and real (σ') parts of the complex conductivity. In the low-frequency region (10^{2}–10^{4} Hz), the PE system shows the highest conductivity. This may be because the internal polarizing electric field causes the ions to concentrate near the electrode interface. The PPE system shows an intermediate conductivity due to the introduction of PVDF-HFP which weakens the piezoelectric polarization ability and the internal electric field. The PP system shows the lowest conductivity due to the lack of ionic liquids. In the high-frequency range (>10^{4} Hz), the rate of increase in σ' becomes significantly more pronounced for all three systems. This change in slope indicates a transition in the dominant electrical behavior—from ionic conduction to dielectric polarization. As the frequency increases, the response of mobile ions becomes increasingly sluggish, and dipolar orientation begins to dominate the material's interaction with the alternating field. This transition is consistent with the dielectric constant results (Figure 2c,d), which likewise show a shift in material behavior from conduction-driven to polarization-driven mechanisms near 10^{4} Hz.

These results reveal a frequency-dependent transition in charge transport mechanisms. All composite systems shift from ion-dominated conduction to dipolar polarization near 10^{4} Hz. This behavior aligns with the RC time constants extracted from the equivalent circuit model. The findings highlight the tunability of dielectric properties through material composition and structural design. Among the three systems, PPE shows well-balanced dielectric and conductive performance across the full frequency range. This suggests its strong potential for optimized multifunctional applications.

2.1 | Multimodal Sensing Ability of Our Sensor

Our soft ionic and piezoelectric composite enabled multimodal sensing of temperature, static strain, and dynamic strain by decoupling the signals in the frequency domain. The equivalent circuit model in Figure 3a illustrates our frequency-domain decoupling strategy for multimodal sensing. At low frequencies (~10^{2} Hz), the impedance response is dominated by dynamic strain (vibration), while mid-frequency (~10^{3} Hz) and high-frequency (~10^{5} Hz) signals primarily reflect temperature induced ionic relaxation and a static strain induced capacitance change. By analyzing the sensor's response across these distinct frequency regimes, individual physical stimuli can be effectively separated for accurate multimodal detection. We use the intrinsic variable charge relaxation time ($\tau = \varepsilon/\sigma = RC$; ε and σ are the dielectric constant and conductivity, respectively), independent of size change, and the extrinsic variable normalized capacitance (C/C_0), sensitive to size change (strain), to achieve precise decoupling of thermal and mechanical signals.

Figure 3b shows the Bode plot of the sensor at different temperatures, which is similar to a previously reported ionic system [13]. Figure S5 shows the temperature-dependent ionic conductivity obtained from Figure 3b. The Figure 3c shows the temperature dependence of the charge relaxation time under different strains ($\varepsilon = 0, 20, 50\%$), confirming static strain independent temperature sensing. Figure 3d shows strain sensing using C/C_0. The variation curves of C/C_0 with uniaxial strain at all temperatures (30 to 50°C) fell on a single curve, which confirms the temperature-independent sensing of static strain. The mechanical durability of the device was confirmed by 100 cycles of 20% strain. The temperature-dependent transport behavior was measured before and after stretching cycles, and negligible changes were observed (Figure S6). In addition, our trimodal sensor showed high humidity-independent sensing across different humidity levels (Figure S7). Although we hypothesized that a hygroscopic ionic liquid could affect stability, the silicone-based encapsulation appears sufficient.

The piezoelectric effect of the composite material is used to sense the dynamic strain. Through a series of control experiments, the decoupling ability of piezoelectric output to temperature and

2365709x, 0, Downloaded from https://advanced.onlinelibrary.wiley.com/doi/10.1002/admt.202502649 by Tno Ris, Wiley Online Library on [05/05/2026]. See the Terms and Conditions (https://onlinelibrary.wiley.com/terms-and-conditions) on Wiley Online Library for rules of use; OA articles are governed by the applicable Creative Commons License

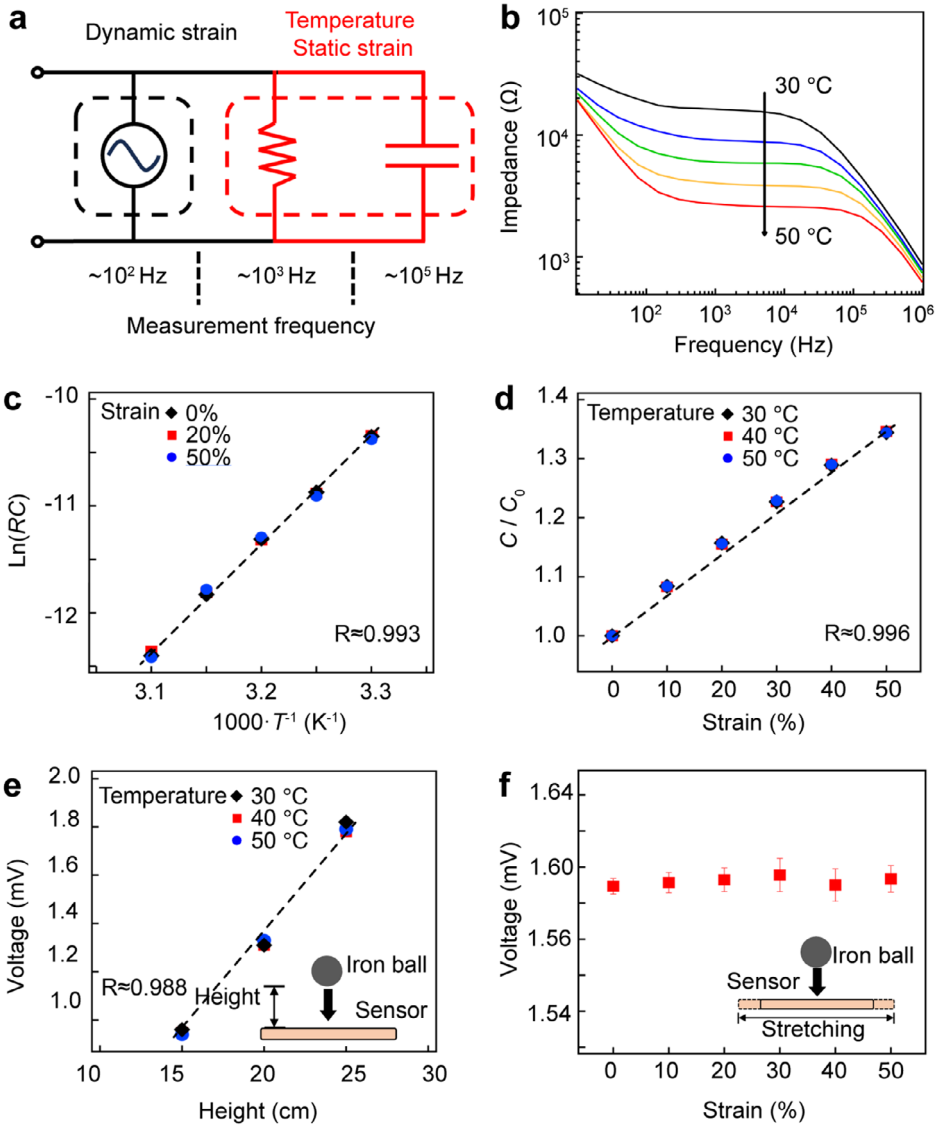


FIGURE 3 | Frequency-dependent decoupling mechanism and multifunctional sensing performance of the composite sensor. (a) Schematic of the frequency-domain decoupling principle: vibration signals are detected in the low-frequency range (~10^2 Hz), temperature effects dominate the mid-frequency (~10^3 Hz), and strain induced impedance changes occur in the high-frequency range (~10^5 Hz). (b) Impedance spectroscopy of the sensor under the temperature from 30 to 50°C. (c) Changes of ln(τ) with respect to T^{-1} (T, temperature) at three tensile strains, with dashed lines representing linear fits, demonstrating that τ is insensitive to static strain and enabling reliable temperature calibration. (d) Changes in C/C_0 as a function of tensile strains at different temperatures, where the dashed lines indicate linear fitting, showing C/C_0 is insensitive to temperature. (e) The piezoelectric output during drop test measurements at temperatures of 30, 40, and 50°C, with linear fits illustrating a consistent calibration relationship and temperature-insensitive dynamic sensing. (f) Output voltage under different stretching strains (0%–50%) with constant impact force, showing a decoupled response to a dynamic mechanical input.

strain is verified. We designed a falling ball experiment to apply dynamic strain input to the sensor under different temperatures and static strain. The sensor is placed under an electromagnet, and the release of the iron ball is controlled by switching the voltage applied to the electromagnet. The amount of dynamic strain applied is determined by the falling height of the iron ball. As shown in Figure 3e, the piezoelectric output voltage of the sensor drops along a consistent main curve at different ambient temperatures (30 to 50°C), indicating that its piezoelectric response is independent from temperature. The piezoelectric response of PVDF-TrFE is caused by the dipole arrangement in its semi-crystalline structure. At temperatures well below the Curie temperature (~130°C), the ambient temperature change is not sufficient to depolarize the composite. Therefore, its piezoelectric coefficient remains stable, ensuring that the piezoelectric output is not sensitive to temperature changes.

In addition, falling ball experiments were performed at room temperature (25°C) while uniaxial transverse static strains (0%–50%) was applied to the sensor (Figure 3f). The piezoelectric output voltage of the sensor drops along a consistent main curve under different static strains, indicating that its piezoelectric response is also independent from static strain. The output signal of piezoelectric materials depends on changes in dipole

2365709x, 0, Downloaded from https://advanced.onlinelibrary.wiley.com/doi/10.1002/admt.202502649 by Tno Ris, Wiley Online Library on [05/05/2026]. See the Terms and Conditions (https://onlinelibrary.wiley.com/terms-and-conditions) on Wiley Online Library for rules of use; OA articles are governed by the applicable Creative Commons License

orientation rather than their absolute state. As a result, they respond to dynamic mechanical stimuli and cannot measure static signals. Under static strain, such as continuous stretching, the initial deformation causes dipole rearrangement, leading to an instantaneous charge separation. However, once the dipoles stabilize in their new orientation, further strain no longer induces additional charge separation [36]. In addition, PVDF-HFP is much softer than PVDF-TrFE. As a result, most of the strain is applied to the PVDF-HFP domains. This allows the material to maintain its piezoelectric activity under large strains.

2.2 | Demonstration and Potential Applications

Based on the verified decoupling of tri-modal signals, we further demonstrate the practical application of our multimodal sensor. We first integrated the sensor into a prosthetic finger (Figure 4a). First, a prosthetic finger equipped with a multimodal sensor was placed on the wrist to demonstrate multimodal sensing (Figure 4b). The skin temperature was measured to be 31.9°C using impedance (detailed data are shown in Table S2). Additionally, the piezoelectric response clearly captures the pulse wave signal. In addition, when the sensor was placed on the neck (Figure 4c), the temperature was found to be 35.5°C. The impedance spectroscopy measured by the sensor is shown in Figure S8. The obtained data were highly consistent with the measured results of the infrared thermometer, indicating that the sensor has good temperature sensing accuracy and reliability (Figure S9).

Furthermore, we fabricated a 3 × 3 sensor array of multimodal sensors onto a prosthetic hand (Figure 4d). Under shear stress, local strain signals near the contact point were enhanced, and temperature increased due to finger heat conduction. Two-dimensional strain and temperature profiles (Figure 4e,f) were generated from normalized capacitance (C/C_0) and charge relaxation time ($\ln(\tau)$) data. The strain distribution showed localized effects of shear stress, while the temperature distribution remained unaffected by strain, demonstrating its stability. The experimental results show that the strain and temperature are concentrated in the shear stress region, verifying the multi-modal response capability of the sensor array and realizing real-time perception and distribution analysis of complex external stimuli.

We also evaluated the human-like ability of multimodal sensors to detect the texture of various materials through their piezoelectric sensing capabilities. A multimodal sensor is set to rub several material surfaces (artificial skin, facial tissue, and copy paper) of different hardness and roughness at a constant speed (10^{-3} m s^{-1}) (Figure 4g,h). During the test, the piezoelectric output of our sensor recorded the dynamic change of the normal force over time. The difference of force signal reflects the obvious difference of surface hardness, roughness and texture of different materials [37]. Specifically, in our study, the force signal on the artificial skin showed high-frequency oscillations with small amplitudes, indicating that the surface is smooth and has some elasticity. In contrast, the facial tissue showed a lower oscillation frequency, and the amplitude of fluctuation was larger than that of the artificial skin, indicating a larger structural inhomogeneity on its surface. This is consistent with previous studies showing that microtextured surfaces induce a moderate level of vibration response in tactile sensors, associated with moderate roughness and deformation characteristics [38–40]. When the sensor slides on the paper surface, the force signal shows the largest peak-to-peak change, and the oscillation frequency is low, indicating that the surface is rough, and the material is rigid, resulting in drastic changes in the contact force. The data show that our multimodal sensor can effectively distinguish the physical properties of different material surfaces through the frequency and amplitude characteristics of the force signal.

3 | Discussion

Table S3 compares the performance of our multimodal sensor with previously reported multimodal devices, highlighting improvements in signal decoupling, stretchability, and integration simplicity [10, 12, 13, 18, 22–25, 41]. To the best of our knowledge, this work represents the first demonstration of decoupling of three signals in a single two-terminal sensor. The decoupling is achieved at the physical mechanism level rather than through device geometry or signal post-processing. Compared to multi-cell sensor architectures, our sensors effectively reduce structural complexity and signal interference. Existing single-device multimodal sensors have significantly advanced multifunctional sensing; however, several intrinsic limitations remained. The number of multimodal sensing modalities with signal decoupling in a single device was limited to two without additional signal processing. Sensors with multimodality more than two often had to rely on artificial intelligence-based signal processing which can mask the reliability or physical meaning of the signals.

In this work, these limitations are addressed by a piezo–ionic multimodal sensing architecture that combines piezoelectric polarization and ionic migration, two fundamentally different physical mechanisms with distinct temporal responses. By exploiting the frequency-dependent characteristics of ionic and piezoelectric signals, multiple stimuli can be effectively decoupled within a single sensing platform, enabling robust and scalable multimodal sensing. In this study, the core of multi-modal detection lies in the strategic integration of ionic and piezoelectric materials, and effective multiple signal decoupling is realized by using charge relaxation time, normalized capacitance, and piezoelectric output as independent variables. In addition, our design utilizes the principle of frequency domain separation, where the electrical responses of different signals occur in different frequency ranges, thereby avoiding signal interference and improving measurement accuracy. While our sensors offer trimodal sensing, they face limitations in challenging environmental conditions. Although our sensors showed high stability across different humidity levels, moisture can still affect device performance after long-term exposure to high humidity. The use of hydrophobic ionic liquids or stretchable encapsulations can fundamentally mitigate this issue [42, 43].

4 | Conclusions

In conclusion, multimodal sensors based on a soft ionic and piezoelectric composite demonstrate strong potential for flexible electronics, particularly in intelligent robotics, continuous health

2365709x, 0, Downloaded from https://advanced.onlinelibrary.wiley.com/doi/10.1002/admt.202502649 by Tno Ris, Wiley Online Library on [05/05/2026]. See the Terms and Conditions (https://onlinelibrary.wiley.com/terms-and-conditions) on Wiley Online Library for rules of use; OA articles are governed by the applicable Creative Commons License

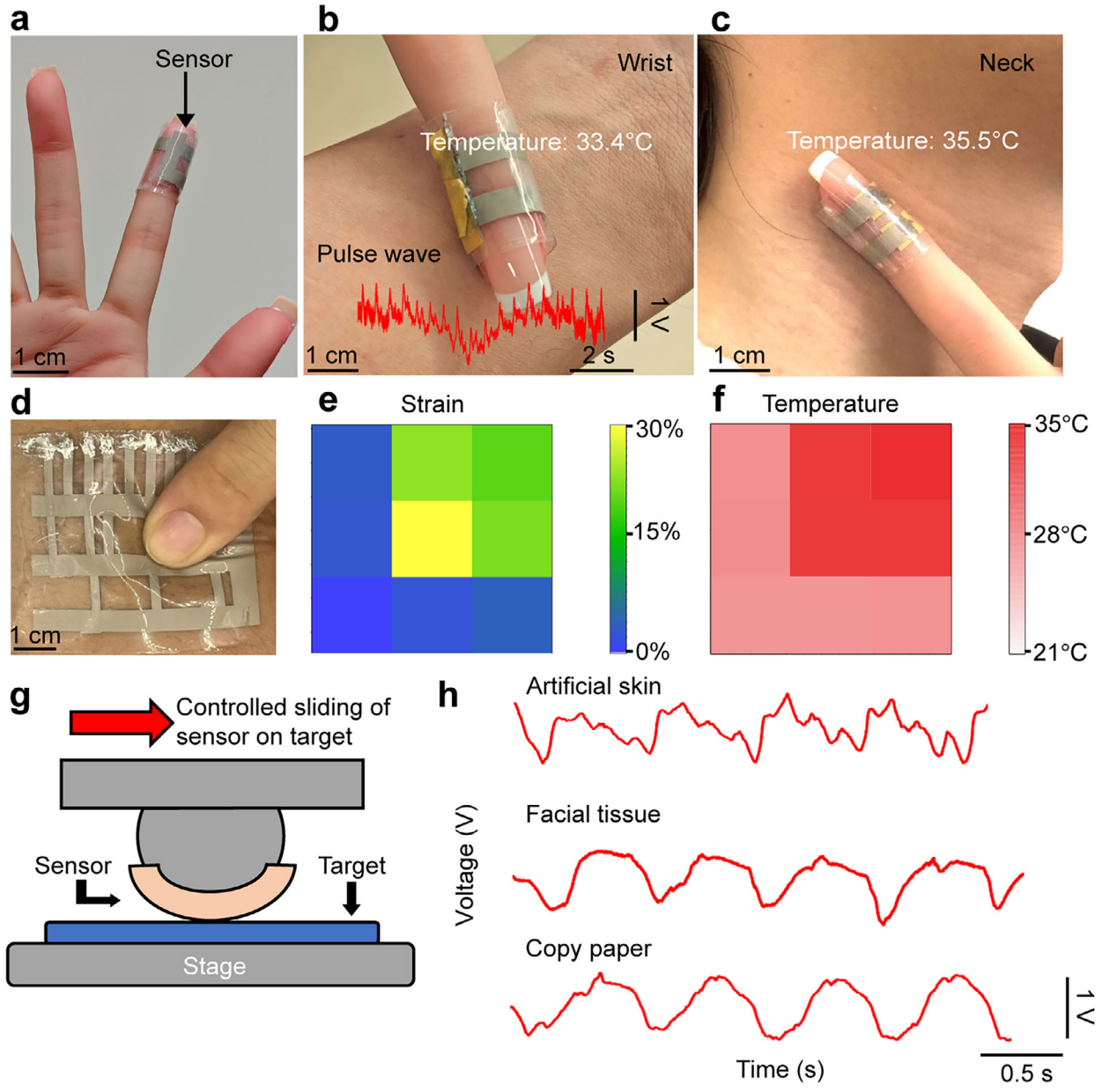


FIGURE 4 | Demonstration of multimodal sensing capabilities. (a) A photograph showing the sensor attached to a prosthetic finger. (b, c) Real-time pulse wave detection and skin temperature monitoring at different sites (31.9°C on the fingertip (b) and 35.5°C near the neck (c)). (d) A photograph of the sensor array applied on skin with finger pressing, used for spatial mapping. (e) Strain mapping result showing spatial distribution of mechanical deformation across the sensor area. (f) Temperature mapping obtained by the sensor, demonstrating thermal gradient detection. (g) A schematic diagram of the sliding test setup used to evaluate surface texture detection. (h) Output voltage profiles generated by sliding across different materials (artificial skin, facial tissue, and copy paper).

monitoring, and human-computer interaction. By integrating temperature, static strain, and dynamic strain sensing capabilities into a single stretchable device, the sensor effectively addresses key challenges in multimodal sensing, such as signal crosstalk and limited sensitivity. This capability enabled real-time, accurate monitoring of physiological signals such as body temperature and pulse waves, as well as tactile perception of surface hardness and roughness. This research combines high sensitivity, mechanical durability and versatility to establish a practical platform for smarter and more efficient medical solutions and intelligent interactive systems.

5 | Method

5.1 | Materials

Glass substrates were purchased from Matsunami glass Ind., Ltd. Silver nanowire (AgNW) ink was purchased from Zhejiang KeChuang Advanced Material Co., Ltd (China) (Product: AW090, 70–105 nm diameter, 1 wt.% in 2-propanol). 2-butanone was purchased from FUJIFILM Wako Pure Chemical Industries. The piezoelectric polymer PVDF-TrFE (Piezotech FC25) (Typical TrFE content: 25 mol%, Curie Temperature: 115°C,

2365709x, 0, Downloaded from https://advanced.onlinelibrary.wiley.com/doi/10.1002/admt.202502649 by Tno Ris, Wiley Online Library on [05/05/2026]. See the Terms and Conditions (https://onlinelibrary.wiley.com/terms-and-conditions) on Wiley Online Library for rules of use; OA articles are governed by the applicable Creative Commons License

Molecular weight: 370–530 kg M^{-1}) was purchased from Arkema. Hydrogenated styrene thermoplastic elastomer (SEBS, Tuftec H1051) was supplied from Asahi Kasei Corporation. PVDF-HFP (FC2176) was purchased from 3 M. EMIM-TFSI was purchased from IOLITEC. Polydimethylsiloxane (PDMS) was purchased from Dow (Product: SILPOT 184). Toluene and 2-propanol were purchased from Fujifilm Wako Pure Chemical Corporation.

5.2 | AgNW Electrodes

The 12 mL AgNW solution was diluted with 6 mL 2-propanol. The AgNW solution was sprayed onto a clean glass slide placed on a hot plate at 80°C and sprayed using an injection pump at a flow rate of 3.0 mL min^{-1} (API GIKEN, API-40RS). The stencil mask was placed on a glass slide to create patterned electrodes. The spray pressure is set to 100 kPa, the distance between the nozzle and the sample is 50 mm, and the scanning speed of the nozzle is 50 mm s^{-1}. The same spraying process was repeated five times. After spraying, the substrate is soaked in deionized water for 10 min. to remove remaining surfactant and then dried. Subsequently, the SEBS solution (0.5 wt.% in toluene) was spincoated on the AgNW layer at 1000 RPM for 1 min. Due to its low concentration, the initial SEBS solution permeates the AgNW infiltration network. After that, a more concentrated SEBS solution (10 wt.% in toluene) was spincoated at 1000 RPM for 1 min. And then thermally annealed at 120°C for 30 min. The SEBS composite was then treated with an O_2 plasma (PIE SCIENTIFIC, Tergeo-plus) (50 W, 60 s), and the PDMS prepolymer (10:1 ratio of prepolymer to curing agent) was then spincoated at 500 RPM for 30 s. The PDMS is then thermally cured at 100°C for 1 h. After curing, the stretchable electrode was delaminated from the glass carrier.

5.3 | Fabrication of Tri-Modal Sensors

PVDF-TrFE, PVDF-HFP, and EMIM-TFSI were mixed at a weight ratio of 10:10:1 and dissolved in a 20 wt.% 2-butanone solution. The mixture was stirred thoroughly at room temperature for 3 h to ensure complete dissolution and homogeneous blending of all components. Dextran solution (10 wt.% in toluene) was spincoated onto the glass substrate at 1500 RPM for 20 s, followed by annealing at 100°C for 5 min. Subsequently, the composite solution was spincoated onto the Dextran-glass substrate at 2000 RPM for 90 s. and then thermally annealed at 135°C for 1 h. Next, a 1 × 1 cm PDMS film (10:1, thickness about 1 mm) was placed on the surface of the composite film and cut along the edge of the PDMS using a knife. Deionized water was then dripped over the incision and left for 5 min to dissolve the Dextran layer. The surface was then dried at 60°C to ensure full adhesion of the composite film to the PDMS layer. Finally, the composite films were transferred to the AgNW electrode using PDMS. After heating at 100°C for 5 min, the PDMS was carefully removed to obtain a sensing active layer uniformly deposited on the AgNW electrode. Finally, laminate the top electrode on top to complete the assembly of the sensor. Because of the conformal contact between the thin viscoelastic layers, the multi-layer material showed good adhesion. To polarize the sample via contact poling, an electric field (100 MV m^{-1}) was applied for 30 min at room temperature. Typically, thickness of the composite active layer was 1.5 μm. Area of the sensors was defined by crossing area of top and bottom AgNW electrodes and was 0.25 cm^2.

5.4 | Electronic Properties of AgNW Layer

The AgNW electrode on SEBS/PDMS substrate was peeled from the glass substrate and fixed onto an X-axis stage (Coms Corporation., PM80B-200X-HQ). The sample was longitudinally stretched at a speed of 0.5 mm s^{-1} using the position controller (Coms Corporation, CP-700D), and conductivity was conducted using the LCR meter (NF Corporation, ZM2376). The resistances of silver nanowires under different strains are shown in Figure S10.

5.5 | Impedance Measurement

Impedance spectroscopy is measured using an impedance analyzer (PalmSens, PalmSense4) and an electrochemical workstation (Bio-Logic VMP3). The applied AC voltage is 0.25 V, and the scanning frequency ranges from 0.1 Hz to 1 MHz. The temperature of the sensor was changed by a hotplate, and after changing the temperature, the impedance is scanned several times until the signal is stable. In order to observe the temperature response of the multimodal sensor in the stretched state, the sensor was adhered onto a glass substrate for impedance measurement. Humidity was controlled by Humidity Control Unit (Kitz Micro Filter Corporation, AHCU-2). Ionic conductivity was calculated from impedance at 10^4 Hz. Unless specifically mentioned, all measurements were conducted at room temperature (20°C) and a relative humidity of 20%.

5.6 | Atomic Force Microscopy

All atomic force microscopy (AFM) images were acquired using a scanning probe microscope (SPM, NANOCUTE / Nanonavi II, Hitachi High-Tech Science, Japan) operated under ambient conditions at room temperature. AFM measurements were performed using silicon self-sensing micro-cantilevers (PRC-DF40P) with a nominal resonance frequency of approximately 324 kHz. The AFM was operated in dynamic (tapping) mode. Images were recorded a with an image resolution of 218 × 218 pixels.

5.7 | Physiological Signal Measurement

The multimodal sensors are fixed on the body surface (wrist, neck) of the volunteers using medical adhesive tape. The impedance spectra are measured using an impedance analyzer (PalmSens, PalmSense4) and an electrochemical workstation (Bio-Logic VMP3). The applied alternating voltage is 0.25 V, and the scanning frequency range is from 0.1 Hz to 1 MHz. The humidity of the measurement environment is maintained at 30%. At the same time, a thermal camera is used to measure the body surface temperature of the experimental area as a control group. A pulse signal was received using an oscilloscope (Keysight, DSOX1204G). This experiment has been approved by the University of Tokyo, Research Ethics Committee

2365709x, 0, Downloaded from https://advanced.onlinelibrary.wiley.com/doi/10.1002/admt.202502649 by Tno Ris, Wiley Online Library on [05/05/2026]. See the Terms and Conditions (https://onlinelibrary.wiley.com/terms-and-conditions) on Wiley Online Library for rules of use; OA articles are governed by the applicable Creative Commons License

(Approval No. 24-230), and written informed consent was obtained from the volunteers.

5.8 | Falling Ball Experiment

An electromagnet was fixed at the top of the experimental setup, with the sensor placed directly underneath. A 15 cm diameter iron ball (~14 g) was used to apply pressure to the sensor. During the experiment, the electromagnet was switched on and off to control the release of the iron ball, while the height of the electromagnet was adjusted to regulate the impact force applied to the sensor. The entire setup was placed inside an oven (Yamato, DKN402) to maintain a controlled experimental temperature. The output voltage was recorded using an oscilloscope (Keysight, DSOX1204G) to analyze the sensor's response under varying impact forces and environmental conditions.

5.9 | Material Identification Experiment

The material identification experiment was assisted by a static friction measuring machine (Trinity-Lab.Inc., i-tester TL201). The multi-modal sensors of this study were fixed on the tactile contactor of the static friction measuring machine, and the experimental objects (artificial leather, copy paper, facial tissue) were fixed on the experimental table of the measuring machine. The sensor was controlled by the measuring machine to slide on the surface of the experimental objects (with a weight of 50 grams, a distance of 10 millimeters, a speed of 10 mm s^{-1}, and repeated sliding 4 times). The oscilloscope (Keysight, DSOX1204G) was used to receive the voltage signal output by the sensor.

Author Contributions

L.W., **Y.L**., and **Y.Z**. fabricated the silver nanowire electrodes. **L.W**., and **V.B**. fabricated the sensor. **L.W**. and **Y.L**. tested the multimodal sensing. **T.F**. and **H.K**. guided the characterization of the sensor's electrical properties. **L.W**., **C.H**., and **S.L**. demonstrated skin-like multimodal sensing in various applications. **P.Z**., and **N.M**. supervised this project. **L.W**., **P.Z**., and **N.M**. wrote the manuscript.

Acknowledgements

The authors thank all volunteers who participated in this research.

Funding

This study was supported by the Japan Society for the Promotion of Science (JP23H01442, JP25KF0021), AMED (JP25tm0524009h0003), Endowed Research Division "Daicel: Electronics for Human Interaction", and the Japan Science and Technology Agency under FOREST (JPMJFR234E), PRESTO (JPMJPR20B7), A-STEP (JPMJTM22BK). The authors thank all volunteers who participated in this research.

Conflicts of Interest

The authors declare no conflicts of interest.

Data Availability Statement

The data that support the findings of this study are available from the corresponding author upon reasonable request.

References

1. R. S. Johansson and Å. B. Vallbo, "Tactile Sensory Coding in the Glabrous Skin of the Human Hand," *Trends in Neurosciences* 6 (1983): 27–32.

2. F. H. Silver, J. W. Freeman, and D. DeVore, "Viscoelastic Properties of Human Skin and Processed Dermis," *Skin Research and Technology* 7 (2001): 18–23.

3. K. Efimenko, M. Rackaitis, E. Manias, A. Vaziri, L. Mahadevan, and J. Genzer, "Nested Self-Similar Wrinkling Patterns in Skins," *Nature Materials* 4 (2005): 293–297.

4. B. Delhaye, A. Barrea, B. B. Edin, P. Lefèvre, and J.-L. Thonnard, "Surface Strain Measurements of Fingertip Skin Under Shearing," *Journal of The Royal Society Interface* 13 (2016): 20150874.

5. M. M. Iskarous and N. Thakor, "E-Skins: Biomimetic Sensing and Encoding for Upper Limb Prostheses," *Proceedings of the IEEE* 107 (2019): 2052–2064.

6. J. Kim, A. S. Campbell, B. E.-F. de Ávila, and J. Wang, "Wearable Biosensors for Healthcare Monitoring," *Nature Biotechnology* 37 (2019): 389–406.

7. T. Someya and M. Amagai, "Toward a New Generation of Smart Skins," *Nature Biotechnology* 37 (2019): 382–388.

8. J. Ge, X. Wang, M. Drack, et al., "A Bimodal Soft Electronic Skin for Tactile and Touchless Interaction in Real Time," *Nature Communications* 10 (2019): 4405.

9. W. Y. Choi, J. H. Kwon, Y. M. Kim, and H. C. Moon, "Multimodal Wearable Ionoskins Enabling Independent Recognition of External Stimuli Without Crosstalk," *Small* 19 (2023): 2301868.

10. M. Jung, K. Kim, B. Kim, K.-J. Lee, J.-W. Kang, and S. Jeon, "Vertically Stacked Nanocellulose Tactile Sensor," *Nanoscale* 9 (2017): 17212–17219.

11. V. Adepu, M. Tathacharya, V. Mattela, and P. Sahatiya, "Development of WS_2/MXene ($Ti_3C_2T_x$) Nanohybrid Based Multi-Functional Textronic Sensor for Non-Invasive Personal Healthcare Monitoring," *Flexible and Printed Electronics* 8 (2023): 015001.

12. M. Cai, Z. Jiao, S. Nie, C. Wang, J. Zou, and J. Song, "A Multifunctional Electronic Skin Based on Patterned Metal Films for Tactile Sensing With a Broad Linear Response Range," *Science Advances* 7 (2021): abl8313.

13. I. You, D. G. Mackanic, N. Matsuhisa, et al., "Artificial Multimodal Receptors Based on Ion Relaxation Dynamics," *Science* 370 (2020): 961–965.

14. Q. Hua, J. Sun, H. Liu, et al., "Skin-Inspired Highly Stretchable and Conformable Matrix Networks for Multifunctional Sensing," *Nature Communications* 9 (2018): 244.

15. J. Zhang, X.-Z. Yuan, C. Song, and H. Wang, *Electrochemical Impedance Spectroscopy in PEM Fuel Cells: Fundamentals and Applications* (Springer, 2009).

16. Y. Jo, Y. Lee, J. Kwon, et al., "3D Active-Matrix Multimodal Sensor Arrays for Independent Detection of Pressure and Temperature," *Science Advances* 11 (2025): ads4516.

17. A. Mascia, A. Spanu, A. Bonfiglio, and P. Cosseddu, "Multimodal Force and Temperature Tactile Sensor Based on a Short-Channel Organic Transistor With High Sensitivity," *Scientific Reports* 13 (2023): 16232.

18. S. Xiao, Y. He, Y. Lu, et al., "An Ultrasensitive Flexible Pressure, Temperature, and Humidity Sensor Based on Structurally Adjustable Nano-Through-Hole Array Films," *Journal of Materials Chemistry C* 11 (2023): 12685–12697.

19. W. Li, K. Lin, L. Chen, et al., "Self-Powered Wireless Flexible Ionogel Wearable Devices," *ACS Applied Materials & Interfaces* 15 (2023): 14768–14776.

20. P. Wu, L. Li, S. Shao, J. Liu, and J. Wang, "Bioinspired PEDOT:PSS-PVDF(HFP) Flexible Sensor for Machine-Learning-Assisted Multimodal Recognition," *Chemical Engineering Journal* 495 (2024): 153558.

2365709x, 0, Downloaded from https://advanced.onlinelibrary.wiley.com/doi/10.1002/admt.202502649 by Tno Ris, Wiley Online Library on [05/05/2026]. See the Terms and Conditions (https://onlinelibrary.wiley.com/terms-and-conditions) on Wiley Online Library for rules of use; OA articles are governed by the applicable Creative Commons License

21. D. Lv, X. Li, X. Huang, et al., "Microphase-Separated Elastic and Ultra-stretchable Ionogel for Reliable Ionic Skin With Multimodal Sensation," *Advanced Materials* 36 (2024): 2309821.

22. L. Li, S. Zhao, W. Ran, et al., "Dual Sensing Signal Decoupling Based on Tellurium Anisotropy for VR Interaction and Neuro-Reflex System Application," *Nature Communications* 13 (2022): 5975.

23. K.-Y. Chun, S. Seo, and C.-S. Han, "A Wearable All-Gel Multimodal Cutaneous Sensor Enabling Simultaneous Single-Site Monitoring of Cardiac-Related Biophysical Signals," *Advanced Materials* 34 (2022): 2110082.

24. D.-L. Wen, Y.-X. Pang, P. Huang, et al., "Silk Fibroin-Based Wearable All-Fiber Multifunctional Sensor for Smart Clothing," *Advanced Fiber Materials* 4 (2022): 873–884.

25. L.-W. Lo, J. Zhao, H. Wan, Y. Wang, S. Chakrabartty, and C. Wang, "A Soft Sponge Sensor for Multimodal Sensing and Distinguishing of Pressure, Strain, and Temperature," *ACS Applied Materials & Interfaces* 14 (2022): 9570–9578.

26. P. Zhao, Y. Song, P. Xie, et al., "All-Organic Smart Textile Sensor for Deep-Learning-Assisted Multimodal Sensing," *Advanced Functional Materials* 33 (2023): 2301816.

27. B.-A. Mei, O. Munteshari, J. Lau, B. Dunn, and L. Pilon, "Physical Interpretations of Nyquist Plots for EDLC Electrodes and Devices," *The Journal of Physical Chemistry C* 122 (2018): 194–206.

28. R. Shyti, P. Nays, R. Vargiolu, and H. Zahouani, "An Innovative Wearable Device for Sensing Mechanoreceptor Activation During Touch," *Scientific Reports* 15 (2025): 9986.

29. Y. Dobashi, D. Yao, Y. Petel, et al., "Piezoionic Mechanoreceptors: Force-induced Current Generation in Hydrogels," *Science* 376 (2022): 502–507.

30. Y. Shim and H. J. Kim, "Dielectric Relaxation and Solvation Dynamics in a Room-temperature Ionic Liquid: Temperature Dependence," *The Journal of Physical Chemistry B* 117 (2013): 11743–11752.

31. C. Gainaru, E. W. Stacy, V. Bocharova, et al., "Mechanism of Conductivity Relaxation in Liquid and Polymeric Electrolytes: Direct Link Between Conductivity and Diffusivity," *The Journal of Physical Chemistry B* 120 (2016): 11074–11083.

32. N. Balar and B. T. O'Connor, "Correlating Crack Onset Strain and Cohesive Fracture Energy in Polymer Semiconductor Films," *Macromolecules* 50 (2017): 8611–8618.

33. M. Klaassen, E. G. de Vries, and M. A. Masen, "Friction in the Contact Between Skin and a Soft Counter Material: Effects of Hardness and Surface Finish," *Journal of the Mechanical Behavior of Biomedical Materials* 92 (2019): 137–143.

34. T. Sekine, K. Ito, Y. Shouji, et al., "Robotic E-Skin for High Performance Stretchable Acceleration Sensor via Combinations of Novel Soft and Functional Polymers," *Applied Materials Today* 33 (2023): 101877.

35. O. L. Anderson and D. A. Stuart, "Calculation of Activation Energy of Ionic Conductivity in Silica Glasses by Classical Methods," *Journal of the American Ceramic Society* 37 (1954): 573–580.

36. S. Chaipo and C. Putson, "Preparation and Enhanced Electrical Breakdown Strength of PVDF-TrFE-CTFE/PVDF-HFP Film Composites," *Journal of Physics: Conference Series* 1719 (2021): 012065.

37. K. Dai, X. Wang, and A. M. Rojas, "Design of a Biomimetic Tactile Sensor for Material Classification," in *2022 International Conference on Robotics and Automation (ICRA)* (IEEE, 2022), 10774–10780.

38. F. B. Kadumudi, M. Jahanshahi, M. Mehrali, et al., "A Protein-based, Water-insoluble, and Bendable Polymer With Ionic Conductivity: A Roadmap for Flexible and Green Electronics," *Advanced Science* 6 (2019): 1801241.

39. P. L. Menezes, Kishore, S. V. Kailas, and M. R. Lovell, "Role of Surface Texture, Roughness, and Hardness on Friction During Unidirectional Sliding," *Tribology Letters* 41 (2011): 1–15.

40. L. Priya, B. Swain, S. Rajput, S. Behera, and S. Parida, "Advances in P(VDF-TrFE) Composites: a Methodical Review on Enhanced Properties and Emerging Electronics Applications," *Condensed Matter* 8 (2023): 105.

41. C. Kwon, S. Lee, C. Won, et al., "Multi-functional and Stretchable Thermoelectric bi_2Te_3 Fabric for Strain, Pressure, and Temperature-sensing," *Advanced Functional Materials* 33 (2023): 2300092.

42. M. Qu, M. Zhu, Y. Lv, et al., "Hydrophobic TPU/CNTs-ILs Ionogel as a Reliable Multimode and Flexible Wearable Sensor for Motion Monitoring, Information Transfer, and Underwater Sensing," *ACS Applied Materials & Interfaces* 16 (2024): 35626–35638.

43. C. Esteves, S. I. C. J. Palma, H. M. A. Costa, et al., "Tackling Humidity With Designer Ionic Liquid-Based Gas Sensing Soft Materials," *Advanced Materials* 34 (2022): 2107205.

Supporting Information

Additional supporting information can be found online in the Supporting Information section.

Supporting File: admt70916-sup-0001-SuppMat.docx.

2365709x, 0, Downloaded from https://advanced.onlinelibrary.wiley.com/doi/10.1002/admt.202502649 by Tno Ris, Wiley Online Library on [05/05/2026]. See the Terms and Conditions (https://onlinelibrary.wiley.com/terms-and-conditions) on Wiley Online Library for rules of use; OA articles are governed by the applicable Creative Commons License